Jost matrices for some analytically solvable potential models

S. N. Ershov

Joint Institute for Nuclear Research, 141980 Dubna, Russia

S. A. Rakityansky

Department of Physics, University of Pretoria, Pretoria, South Africa

A family of analytically solvable potential models for the one- and two-channel problems is considered within the Jost matrix approach. The potentials are chosen to be constant in the interior region and to have different asymptotic behavior (tails) at large distances. The migration of the S-matrix poles on the Riemann surface of the energy, caused by variations of the potential strength, is studied. It is demonstrated that the long-range ($\sim 1/r^2$) tails and Coulomb potential ($\sim 1/r$) cause an unusual behavior of the S-matrix poles. It is found that in the two-channel problem with the long-range potentials the S-matrix poles may appear at complex energies on the physical Riemann sheet. The Coulomb tail not only changes the topology of the Riemann surface, but also breaks down the so-called mirror symmetry of the poles in both the single-channel and the two-channel problems.

I. INTRODUCTION

Theoretical interpretation of experimentally measured scattering cross sections often requires considering the physical system at unphysical complex energies. Such a consideration allows one to reveal the spectral singularities of the S matrix. If these singularities are close to the real energies, they can strongly influence the energy dependence of the observables. In particular, various irregularities (e.g., zigzags) of the cross-section curves can be understood as the effects of such S-matrix poles at complex energies.

The S matrix is a multivalued function of the complex energy-variable E. This means that a single value of E corresponds to several (or even infinite in the case of Coulomb forces) different values of $S(E)$. As a result, the function $S(E)$ is defined not on the single E plane, but on a multilayered Riemann surface where each layer (sheet) is a copy of the E plane and corresponds to a separate value of S. Each sheet of the Riemann surface has its own real axis. All of them are cut along the positive halves of these axes and the edges of the cuts of different sheets are interconnected in such a way that going around the threshold energies (which are the branch points) brings us from one layer to the other in accordance with the analytic structure of the function $S(E)$.

The topology of the Riemann surface is simple only in the single-channel problem with a short-range potential, where it consists of just two sheets (the physical and nonphysical ones) with the square-root branch point at $E = 0$. In this simple problem the function $S(E)$ is double-valued because it actually depends on the momentum k, and when calculating the square root $k \sim (\pm\sqrt{E})$ we can choose either the positive or negative sign. The physical sheet corresponds to such a choice of this sign that $\operatorname{Im} k \geqslant 0$, and on the nonphysical sheet $\operatorname{Im} k < 0$.

Even in the single-channel problem, if the particles have nonzero charges, the point $E = 0$ becomes the square-root and the logarithm branch point at the same time, the number of sheets becomes infinite, and the topology of the surface becomes spiral (for details see Ref. [1]). When the number of channels is more than one, the intricate interconnections of the sheets make its topology very complicated.

The physical scattering energies ($E > 0$) are on the upper edge of the cut of the physical sheet, which is connected to the lower edge of the cut of the nonphysical sheet. Only those S-matrix poles that are close to these scattering energies may noticeably influence the observables. This means that only poles that are slightly below the real axis (i.e., on the nonphysical sheet) and that are slightly above this axis on the physical sheet can affect the observables.

Long ago, using the causality principle, it was proved that on the physical sheet of the Riemann surface the S matrix can have poles only at bound-state energies, $E < 0$ [2]. This means that there are no poles above the scattering energies, and only those below the real axis, i.e., the resonances, influence the scattering process. However, the proof in Ref. [2] was given only for a single-channel problem with a short-range potential and a generalization to the long-range forces or to multichannel problems is absent. Despite this, it became a common belief that there are no poles on the physical sheet no matter how complicated the problem is. This belief is based on common sense and intuition, which are not to be always trusted.

An example of misunderstanding caused by such a belief, is the confusion around the so-called shadow pole associated with the two-channel ($n\alpha$ and dt) resonance state $^5\mathrm{He}^*(3/2^+)$ which is formed at ≈ 50 keV in the dt collision.

Using the R-matrix analysis of experimental data as well as some approximate calculations, several research groups

[3–7] came to the conclusion that, in addition to the normal resonant pole on the nonphysical sheet, it should be another (shadow) pole without which the data are not fit. The shadow pole has been placed on one of the remote sheets (different assignments have been suggested by different authors). It is a long way around the branch point from this shadow pole to the scattering energy and an explanation why such a remote pole influences the observable cross section is needed. The possibility that the shadow pole could be just above the real axis on the physical sheet has not been considered.

First of all, note that there is no rigorous definition of the shadow poles. It is assumed that in some cases the S-matrix poles located somewhere on the Riemann surface but not on the same sheet as the resonances can also influence the observable cross section. If such poles do exist, they are termed "shadow poles." The most simple and logical would be to expect them to be on the physical sheet just above the real axis. This however "contradicts" the causality principle.

Recently we reanalyzed [1] the data for the nuclear system ^{5}He in the state $3/2^+$ using the semi-analytic representation of the multichannel Jost matrix with proper analytic structure suggested in Ref. [8]. It was found that indeed there is the shadow pole, but it is on the physical sheet. A similar analysis [9] of the system ^{8}B(0^+) also revealed the shadow pole on the physical sheet.

These findings made us doubt the validity of the ban on the existence of the poles on the physical sheet in a multichannel problem. The only convincing way to disprove the ban is to find a counterexample where everything can be solved exactly. This is the main aim of the present paper.

As such an example, we chose the two-channel potentials, which are of simple square-well shape up to certain distance R. Beyond R the diagonal potentials have a centrifugal barrier or a repulsive Coulomb tail. For such potentials it is not difficult to solve the radial Schrödinger equation exactly and to obtain analytic expressions for the Jost matrices. The corresponding S matrix is then obtained as the "ratio" of two Jost matrices. Varying the parameters of the potential, we can trace the movements of the S-matrix poles and check if any of them go to the "prohibited" domain.

To be methodical and consistent, we consider (within the same approach) a sequence of the problems with increasing complexity. Starting with the simplest single-channel square-well potential, we add to it the centrifugal tail, then the Coulomb tail, then make it two-channel with either the centrifugal or with the Coulomb tails. It turned out that the only problem where the "forbidden" poles on the physical sheet appear, is the two-channel problem with the centrifugal tail. This finding is an explicit example where the common belief in nonexistence of the complex poles on the physical sheet is disproved.

The paper is organized as follows. In Sec. II we define the family of one- and two-channel potential models and find analytical expressions for the S matrix and wave functions using the Jost matrix method. In Sec. III we explore the patterns of the movement of the S-matrix poles for different models and discuss their general properties. Appendixes contain supplemental material that illuminates some important calculation details.

II. FORMALISM

Consider a system of two spinless bodies that interact via a spherically symmetric potential U. If $|i\rangle$ describes the internal states of the bodies and μ is the reduced mass (we assume it to be the same in all the channels), then introducing the reduced potential matrix $V_{i,j}$,

$$\frac{2\mu}{\hbar^2} \langle \vec{r}', i | U | \vec{r}, j \rangle = \delta(\vec{r}' - \vec{r}) V_{i,j}(r), \tag{1}$$

where $\vec{r}$ is the relative coordinate, and performing the standard partial-wave decomposition, we obtain the following system of Schrödinger equations for the radial components, $u_{i,j}(k, r)$, of the wave function of the relative motion:

$$u''_{i,j}(k, r) + \left[k^2 - \epsilon_i - \frac{\ell_i(\ell_i + 1)}{r^2} \right] u_{i,j}(k, r)$$
$$- \sum_n V_{i,n}(r) u_{n,j}(k, r) = 0. \tag{2}$$

Here k is the wave number corresponding to the center-of-mass energy E via the relation $k^2 = (2\mu/\hbar^2)E$, and the parameters ϵ_i are expressed as $\epsilon_i = (2\mu/\hbar^2)E_i$ in terms of the threshold energies E_i of the channels $i = 1, 2, \ldots$. The potential matrix is symmetric, $V_{i,j} = V_{j,i}$.

Our aim is to analytically solve Eqs. (2) for a family of one- and two-channel potentials, and then to study the properties of these solutions at complex energies. Although the equations have a simple linear dependence on E, their solutions, $u_{i,j}$, have a more complicated dependence on this parameter. They depend on E via the channel momenta,

$$k_i = \pm\sqrt{k^2 - \epsilon_i}, \tag{3}$$

and (if the Coulomb forces are present) on their logarithms,

$$\ln(k_i) = \ln |k_i| + i[\arg(k_i) + 2\pi m_i],$$
$$m_i = 0, \pm 1, \ldots. \tag{4}$$

This is because the solutions are determined not only by the equations but also by the boundary conditions, which at infinity involve the ingoing and outgoing spherical waves (see Eq. (9) further down) or their combinations. These waves explicitly depend on k_i and $\ln(k_i)$.

Since for a single value of E there are two possible values of each k_i and infinite number of possible $\ln(k_i)$, the solutions $u_{i,j}$ (as well as all the quantities associated with them) are multivalued functions of E. In particular, the S matrix is such a multivalued function of the complex variable E. It is therefore defined on a multilayered Riemann surface with the square-root and logarithm branch points at every threshold energy E_i. On such a surface the S matrix is a single-valued function of the energy.

We denote the sheets of the Riemann surface by the signs of Im k_i and by the integer numbers m_i, i.e., by the logarithmic indices defined in Eq. (4).

In total, due to the square-root branch points, there are 2^N possible sign combinations of the channel momenta, where N is the number of channels. If the Coulomb interaction is present, the number of the Riemann sheets becomes infinite because the logarithm indices in Eq. (4) may have infinitely many different values. It is customary to cut the k plane from

$-\infty$ to zero and define the principal branch of the logarithm as a part of the function (4) that corresponds to $m_i = 0$ and $-\pi \leqslant \arg(k_i) < \pi$. The energy sheet where $\operatorname{Im} k_i > 0$ and $m_i = 0$ is called physical with respect to the channel i. In the two-channel problem, we simply call the sheet physical if it is physical with respect to both channels.

A. Analytically solvable models

To make our models analytically solvable, we divide the configuration space into the internal and external regions (within and outside a sphere of the radius R) and in these regions use simple potentials for which the problem can be easily solved. What then remains is to smoothly match the internal and external solutions and their derivatives at $r = R$.

We only consider one- and two-channel models with the S-wave interactions. In the internal region, $r \leqslant R$, the potential is taken to be constant, i.e., $V_{i,i}(r) = V_i$ and $V_{1,2}(r) = V_{2,1}(r) = \Delta$, where both the diagonal and off-diagonal elements, V_i and Δ, are r independent. In the external region, $r > R$, we assume that the coupling potentials among the channels disappear and the potential matrix becomes diagonal, $V_{i,j} \sim \delta_{ij}$. The following three different external potentials (tails) are considered:

(1) zero potential that leads to the free exponential solutions;
(2) "centrifugal barrier" potential, $V_{i,i}(r) = \ell(\ell + 1)/r^2$, for which the solutions are the Ricatti-Hankel functions of the integer order ℓ;
(3) the Coulomb potential $V_{i,i}(r) \sim 1/r$ that gives the Coulomb wave functions for $r > R$.

The first choice is the simplest one and is a particular case of the second with $\ell = 0$. For both of them the Riemann surface has only the square-root branch points at E_i. The Coulomb tail in the third choice leads to a different topology of the Riemann surface due to an additional logarithmic branch point.

B. Two-channel problem

Each column of the matrix $u_{i,j}$ is a separate solution of Eq. (2). In general, a system of N second-order differential equations (2) has $2N$ linearly independent column-solutions, but only half of them are regular at $r = 0$. For $N = 2$, there are two linearly independent regular columns. They therefore form a square matrix

$$\hat{u} = \begin{pmatrix} u_{1,1} & u_{1,2} \\ u_{2,1} & u_{2,2} \end{pmatrix}. \tag{5}$$

These two columns constitute a basis in the space of all possible solutions that are regular at the origin. In other words, any physical solution (which is always a single column) is a linear combination of the two columns of matrix (5). We denote a single column-solution by the "hat" above the letter with a single subscript,

$$\hat{u}_\alpha(k, r) = \begin{bmatrix} u_{1,\alpha}(k, r) \\ u_{2,\alpha}(k, r) \end{bmatrix}.$$

The columns differ from one another by the boundary conditions.

In the external region ($r > R$), the system of equations (2) decouples,

$$u_{i,\alpha}''(k, r) + \left[k_i^2 - V_{i,i}(r)\right]u_{i,\alpha}(k, r) = 0. \tag{6}$$

It is convenient to consider here the so-called Jost solutions that asymptotically behave as pure spherical waves [10]. At $r > R$ there is no requirement of regularity. We therefore take into account all four independent column-solutions, which are combined in two square matrices (denoted by the superscripts "+" and "−"),

$$\hat{f}^{(\pm)}(k, r) = [\hat{f}_1^{(\pm)}(k, r), \hat{f}_2^{(\pm)}(k, r)], \tag{7}$$

which are diagonal thanks to the decoupling of the differential equations at $r > R$,

$$\hat{f}^{(\pm)}(k, r) = \begin{bmatrix} \chi^{(\pm)}(k_1, r) & 0 \\ 0 & \chi^{(\pm)}(k_2, r) \end{bmatrix}, \tag{8}$$

where

$$\chi^{(\pm)}(k_i, r) \overset{r \to \infty}{\longrightarrow} \exp(\pm i k_i r)$$
$$\overset{r \to \infty}{\longrightarrow} \exp\{\pm i[k_i r - \eta_i \ln(2k_i r)]\}. \tag{9}$$

Here, the second line corresponds to the case when the ith channel has the Coulomb potential at $r > R$, and η_i is the Sommerfeld parameter. The solutions $\chi^{(\pm)}(k_i, r)$ satisfy the following Wronskian relation $[W(f, g) = fg' - f'g]$:

$$W[\chi^{(+)}(k_i, r), \chi^{(-)}(k_i, r)] = -2ik_i. \tag{10}$$

The Jost solutions constitute a complete basis in the external region. Therefore, in this region any other solution can be written as their linear combination.

In the internal region the column-solution $\hat{u}_\alpha(k, r)$ obeys the system of two coupled radial equations,

$$\begin{pmatrix} u_{1,\alpha} \\ u_{2,\alpha} \end{pmatrix}'' + \begin{pmatrix} k^2 & 0 \\ 0 & k^2 \end{pmatrix}\begin{pmatrix} u_{1,\alpha} \\ u_{2,\alpha} \end{pmatrix}$$
$$= \begin{pmatrix} \varepsilon_1 + V_1 & \Delta \\ \Delta & \varepsilon_2 + V_2 \end{pmatrix}\begin{pmatrix} u_{1,\alpha} \\ u_{2,\alpha} \end{pmatrix}. \tag{11}$$

The symmetric matrix on the right side of Eq. (11) couples different channels and can be diagonalized by the orthogonal matrix $\hat{O}$,

$$\begin{pmatrix} \varepsilon_1 + V_1 & \Delta \\ \Delta & \varepsilon_2 + V_2 \end{pmatrix} = \hat{O} \cdot \hat{w} \cdot \hat{O}^T$$
$$= \begin{pmatrix} \cos\theta & -\sin\theta \\ \sin\theta & \cos\theta \end{pmatrix}\begin{pmatrix} \omega_1 & 0 \\ 0 & \omega_2 \end{pmatrix}$$
$$\times \begin{pmatrix} \cos\theta & \sin\theta \\ -\sin\theta & \cos\theta \end{pmatrix}, \tag{12}$$

where the diagonal matrix elements ω_1 and ω_2 as well as the mixing angle θ are defined by the following expressions:

$$\omega_{1,2} = \frac{1}{2}(\varepsilon_1 + V_1 + \varepsilon_2 + V_2 \pm \Gamma),$$

$$\Gamma = \sqrt{(\varepsilon_1 + V_1 - \varepsilon_2 - V_2)^2 + 4\Delta^2},$$

$$\sin 2\theta = \frac{2\Delta}{\Gamma}.$$

Multiplying Eq. (11) from the left by $\hat{O}^T$ and inserting the unit matrix $I = \hat{O}\hat{O}^T$ between the matrices on its right-hand side, we obtain the uncoupled system of equations for the new unknown column-solution $\hat{v}_\alpha = \hat{O}^T \hat{u}_\alpha$:

$$\begin{bmatrix} v_{1,\alpha}(k,r) \\ v_{2,\alpha}(k,r) \end{bmatrix}'' + \begin{bmatrix} \lambda_1^2 v_{1,\alpha}(k,r) \\ \lambda_2^2 v_{2,\alpha}(k,r) \end{bmatrix} = 0, \qquad (13)$$

where $\lambda_i^2 = k^2 - w_i$ are the eigenfrequencies. Equations (13) can be easily solved. There are four independent solutions:

$$\hat{v}_\alpha = \begin{pmatrix} e^{+i\lambda_1 r} \\ 0 \end{pmatrix}, \begin{pmatrix} e^{-i\lambda_1 r} \\ 0 \end{pmatrix}, \begin{pmatrix} 0 \\ e^{-i\lambda_2 r} \end{pmatrix}, \begin{pmatrix} 0 \\ e^{+i\lambda_2 r} \end{pmatrix}.$$

The original solutions can be found via the inverse transformation, $\hat{u}_\alpha(k,r) = \hat{O}\hat{v}_\alpha(k,r)$. The four solutions thus obtained are denoted by different combinations of the signs in the superscripts $(\pm)$ and the two values of the subscript α:

$$\hat{u}_1^{(\pm)}(k,r) = \begin{pmatrix} \cos\theta \\ \sin\theta \end{pmatrix} \exp(\pm i\lambda_1 r), \qquad (14)$$

$$\hat{u}_2^{(\pm)}(k,r) = \begin{pmatrix} -\sin\theta \\ \cos\theta \end{pmatrix} \exp(\pm i\lambda_2 r). \qquad (15)$$

It should be noted that the four independent solutions (14) and (15) constitute a complete basis. Therefore, not only regular, but any solution in the internal region can be written as a linear combination of the four columns (14), (15). In particular, the Jost solutions at $r \leqslant R$ can be obtained by smooth matching of the external solutions (7) with such a combination at $r = R$. Equalizing the functions and their derivatives at the boundary between the regions, we find the four combination coefficients. This gives for $r \leqslant R$ the following Jost solutions:

$$\hat{f}_1^{(\pm)}(k,r) = \begin{pmatrix} \cos^2\theta\,\psi_{1,1}^{(\pm)} + \sin^2\theta\,\psi_{2,1}^{(\pm)} \\ \sin\theta\cos\theta[\psi_{1,1}^{(\pm)} - \psi_{2,1}^{(\pm)}] \end{pmatrix}, \qquad (16)$$

$$\hat{f}_2^{(\pm)}(k,r) = \begin{pmatrix} \sin\theta\cos\theta[\psi_{1,2}^{(\pm)} - \psi_{2,2}^{(\pm)}] \\ \sin^2\theta\,\psi_{1,2}^{(\pm)} + \cos^2\theta\,\psi_{2,2}^{(\pm)} \end{pmatrix}, \qquad (17)$$

where the functions $\psi_{i,j}^{(\pm)}(r)$ are given by

$$\psi_{i,j}^{(\pm)}(r) = \cos[\lambda_i(R-r)]\chi^{(\pm)}(k_j,R)$$
$$- \frac{1}{\lambda_i}\sin[\lambda_i(R-r)]\chi^{(\pm)\prime}(k_j,R). \qquad (18)$$

The Jost solutions satisfy the following matrix Wronskian relation $[W(\hat{f},\hat{g}) = \hat{f}^T\hat{g}' - \hat{f}^{T\prime}\hat{g}$, superscript "$T$" indicates the transposed matrix]:

$$W[\hat{f}^{(+)}(k,r), \hat{f}^{(-)}(k,r)] = -2i\hat{k}, \qquad (19)$$

where $\hat{k}$ is the diagonal matrix with the elements $\hat{k}_{i,j} = \delta_{i,j}k_j$. Generally speaking, the Jost solutions are irregular at the origin, namely, behave as $\sim r^{-\ell}$. However, for the case of $\ell = 0$ (which we consider) they have finite values at $r = 0$.

Among all possible regular solutions we, following Ref. [11], consider the solution $\hat{\varphi}(k,r)$ which is a square matrix obeying the boundary conditions at the origin, which do not depend on the energy,

$$\hat{\varphi}(k,0) = \hat{0}, \quad \hat{\varphi}'(k,0) = \hat{1}. \qquad (20)$$

Since the Jost solutions constitute a complete basis in the space of all the solutions, $\hat{\varphi}(k,r)$ can be written as their linear combination,

$$\hat{\varphi}(k,r) = \hat{f}^{(+)}(k,r)\hat{c}^{(+)} + \hat{f}^{(-)}(k,r)\hat{c}^{(-)}. \qquad (21)$$

The matrix coefficients $\hat{c}^{(\pm)}$ can be found by calculating the corresponding Wronskians. Indeed, using Eq. (19), we obtain

$$W[\hat{f}^{(\pm)}(k,r), \hat{\varphi}(k,r)] = \mp 2i\hat{k}\hat{c}^{(\mp)}. \qquad (22)$$

The Jost matrices can be defined as the above Wronskians (which are independent of r):

$$\hat{f}^{(\pm)T}(k) = W[\hat{f}^{(\pm)}(k,r), \hat{\varphi}(k,r)]$$
$$= \hat{f}^{(\pm)T}(k,0), \qquad (23)$$

where the second equality follows from the boundary conditions (20). The explicit forms of the Jost matrices $\hat{f}^{(\pm)}(k)$ are given by Eqs. (16) and (17) taken at $r = 0$. Therefore the coefficients $\hat{c}^{(\pm)}$ are

$$\hat{c}^{(\pm)} = \mp\frac{i}{2}\hat{k}^{-1}\hat{f}^{(\mp)T}(k), \qquad (24)$$

and for the regular solution we obtain $[r \in [0,\infty)]$:

$$\hat{\varphi}(k,r) = \frac{i}{2}[\hat{f}^{(-)}(k,r)\hat{k}^{-1}\hat{f}^{(+)T}(k)$$
$$- \hat{f}^{(+)}(k,r)\hat{k}^{-1}\hat{f}^{(-)T}(k)]. \qquad (25)$$

To find out how the introduced Jost matrices are related to the S matrix, it is convenient to rewrite this form of $\hat{\varphi}(k,r)$ in such a way that it explicitly includes the functions $\hat{W}^{(\text{in/out})}(k,r) = \pm\hat{f}^{(\mp)}(k,r)\hat{k}^{-1/2}$ that asymptotically behave as the incoming and outgoing spherical waves, normalized to the unit flux. To this end we multiply Eq. (25) from the right by the unit matrix

$$I = [\hat{f}^{(+)T}(k)]^{-1}\hat{k}^{1/2}[\hat{f}^{(+)}(k)\hat{k}^{-1/2}]^T,$$

which gives

$$\hat{\varphi}(k,r) = \frac{i}{2}\{\hat{f}^{(-)}(k,r)\hat{k}^{-1/2} - \hat{f}^{(+)}(k,r)\hat{k}^{-1/2}$$
$$\times \hat{k}^{-1/2}\hat{f}^{(-)T}(k)[\hat{f}^{(+)T}(k)]^{-1}\hat{k}^{1/2}\}[\hat{f}^{(+)}(k)\hat{k}^{-1/2}]^T,$$

i.e.,

$$\hat{\varphi}(k,r) = \frac{i}{2}[\hat{W}^{(\text{in})}(k,r) + \hat{W}^{(\text{out})}(k,r)\hat{S}(k)]$$
$$\times [\hat{f}^{(+)}(k)\hat{k}^{-1/2}]^T,$$

where the S matrix whose open channel submatrix is unitary at real positive energy, is given by

$$\hat{S}(k) = \hat{k}^{-1/2}\hat{f}^{(-)T}(k)[\hat{f}^{(+)T}(k)]^{-1}\hat{k}^{1/2}. \qquad (26)$$

Since all the matrices in Eq. (26) have the dimensions (2×2), it is not difficult to perform the inversion and all the multiplications explicitly. This gives

$$\hat{S}(k) = \frac{1}{\det\hat{f}^{(+)}(k)} \begin{pmatrix} A & B \\ B & C \end{pmatrix}. \qquad (27)$$

Here, the determinant of the Jost matrix, $\det\hat{f}^{(+)}(k)$, is equal to

$$\det\hat{f}^{(+)}(k) = \cos^2\theta\,\psi_{1,1}^{(+)}(0)\psi_{2,2}^{(+)}(0) + \sin^2\theta\,\psi_{1,2}^{(+)}(0)\psi_{2,1}^{(+)}(0). \qquad (28)$$

Its zeros correspond to the S-matrix poles. The elements of the matrix (27) are given by

$$A = \chi^{(-)}(k_1 R)\chi^{(+)}(k_2 R)D^{(-,+)},$$
$$B = 2i\sqrt{k_1 k_2}R\sin\theta\cos\theta(s_1 c_2 - c_1 s_2), \qquad (29)$$
$$C = \chi^{(+)}(k_1 R)\chi^{(-)}(k_2 R)D^{(+,-)},$$

where $s_i = \sin(\lambda_i R)/(\lambda_i R)$, $c_i = \cos(\lambda_i R)$, and the coefficients $D^{(\pm,\pm)}$ can be found as

$$D^{(\pm,\pm)} = c_1 c_2 + s_1 s_2 L_1^{(\pm)}L_2^{(\pm)} - L_1^{(\pm)}(\cos^2\theta s_1 c_2 + \sin^2\theta c_1 s_2)$$
$$- L_2^{(\pm)}(\cos^2\theta c_1 s_2 + \sin^2\theta s_1 c_2), \qquad (30)$$

with

$$L_i^{(\pm)} = R\chi^{(\pm)\prime}(k_i R)/\chi^{(\pm)}(k_i R). $$

When looking for the S-matrix poles and tracing their migration on the Riemann surface, we only need to look for and trace the zeros of the determinant (28). An alternative expression for this determinant is

$$\det \hat{f}^{(+)}(k) = \chi^{(+)}(k_1 R)\chi^{(+)}(k_2 R)D^{(+,+)}. \qquad (31)$$

The unitarity of the S matrix at the real positive energy can be checked by straightforward calculations. The partial cross sections $\sigma_{i\to j}$ for S-wave scattering from the ith to jth channels are given by the standard expression

$$\sigma_{i\to j} = \frac{\pi}{k_i^2}|S_{i,j} - \delta_{i,j}|^2. \qquad (32)$$

C. Single-channel problem

The more simple formulas for the single-channel case are obtained from the corresponding equations of the preceding section if in the matrix of the potential we only retain the first element $V_{1,1}(r)$,

$$V_{1,1}(r) = \begin{cases} V_1, & r \leqslant R \\ 0, & r > R \quad (*) \\ \sigma/r^2, & r > R \quad (**) \\ 2k\eta/r, & r > R \quad (***), \end{cases} \qquad (33)$$

where V_1 is a constant value of the potential in the internal region, and there are three choices, $(*)$, $(**)$, and $(***)$, of the potential tail in the external region. Here $\sigma > 0$ is the strength of the external centrifugal barrier. In the calculations we chose $\sigma = 6$, which corresponds to $\ell = 2$ in $\ell(\ell + 1)/r^2$, i.e., to the quadrupole barrier. The Sommerfeld parameter $\eta = 1/(ak)$ corresponds to the Coulomb interaction between two particles with charges eZ_1 and eZ_2, where $a = \hbar^2/(\mu e^2 Z_1 Z_2)$ is the nuclear Bohr radius. The potential (33) is schematically depicted in Fig. 1.

The integer value of ℓ in $\sigma = \ell(\ell + 1)$ of the choice $(**)$ in the potential (33) does not change the topology of the Riemann surface, i.e., it still has the same square-root branch point as in the simplest case $(*)$. In contrast to that, in the case $(***)$ the Coulomb tail drastically changes the Riemann surface because the threshold energy, $E = 0$, becomes not only the square-root but also the logarithm branch point. As a result, the Riemann surface becomes spiral with an infinite number of sheets.
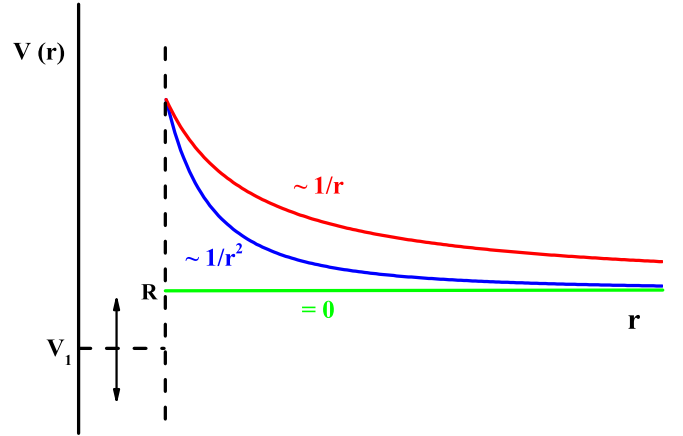

FIG. 1. The potentials used in the model, consist of a constant (flat) potential at $r \leqslant R$ with the variable depth V_1 and three different tails at $r > R$: $(*)$ short-range (identical zero), $(**)$ centrifugal potential $(\sim 1/r^2)$, $(***)$ Coulomb potential $(\sim 1/r)$.

In the external region, $r > R$, the two Jost solutions, $\chi^{(\pm)}(kr)$, for the three different choices of the tail in (33) are $(*)$ the Ricatti-Hankel functions $h_0^{(\pm)}(kr)$; $(**)$ the Ricatti-Hankel functions $h_2^{(\pm)}(kr)$; and $(***)$ the Coulomb functions $\mathcal{H}_{\eta,0}^{(\pm)}(kr)$ of zero order,

$$\chi^{(\pm)}(z) = \begin{cases} h_0^{(\pm)}(z) = e^{\pm iz} & (*) \\ h_2^{(\pm)}(z) = (3/z^2 \mp 3i/z - 1)e^{\pm iz} & (**) \\ \mathcal{H}_{\eta,0}^{(\pm)}(z) = e^{\mp i\sigma_{\eta,0}}[G_{\eta,0}(z) \pm iF_{\eta,0}(z)] & (***), \end{cases}$$
$$(34)$$

where $z = kr$, $F_{\eta,0}(z)$, and $G_{\eta,0}(z)$ are the standard regular and irregular Coulomb functions of the zero order. The S-wave Coulomb phase shift, $\sigma_{\eta,0}$, is given by

$$\sigma_{\eta,0} = \frac{1}{2i}[\ln\Gamma(1 + i\eta) - \ln\Gamma(1 - i\eta)]. \qquad (35)$$

For the single-channel case the S matrix (26) becomes a simple ratio of the two Jost functions,

$$S(k) = f^{(-)}(k)/f^{(+)}(k),$$

and its poles are just zeros of $f^{(+)}(k)$. The Jost functions can be found using Eq. (23), i.e., by taking the Jost solutions (16) at $r = 0$. In this column we should only take the top element with $\theta = 0$. In this way we obtain

$$f^{(\pm)}(k) = \psi_{1,1}^{(\pm)}(0),$$

where $\psi_{1,1}^{(\pm)}$ is given by Eq. (18). Therefore,

$$f^{(\pm)}(k) = \chi^{(\pm)}(kR) - \frac{\sin(\lambda R)}{\lambda}\chi^{(\pm)\prime}(kR), \qquad (36)$$

with $\lambda^2 = k^2 - V_1$. The Jost solutions and their derivatives at $r = R$ that are needed in Eq. (36) can be found using one of the three choices given in Eq. (34).

From the explicit expressions (36) for the Jost functions we can establish the symmetry relations for them with respect to changing sign or complex conjugation of the momentum, i.e.,

the symmetry relations at different points on the complex k plane. It is clear that in the cases (∗) and (∗∗) we have

$$h_\ell^{(\pm)}(z) = h_\ell^{(\mp)}(-z) = [h_\ell^{(\mp)}(z^\star)]^\star = [h_\ell^{(\pm)}(-z^\star)]^\star.$$

Exactly the same relations are valid for

$$g_\ell^{(\pm)}(z) = z\frac{d}{dz}h_\ell^{(\pm)}(z),$$

i.e.,

$$g_\ell^{(\pm)}(z) = g_\ell^{(\mp)}(-z) = [g_\ell^{(\mp)}(z^\star)]^\star = [g_\ell^{(\pm)}(-z^\star)]^\star.$$

At the same time the values of $\cos(\lambda R)$ and $\sin(\lambda R)/\lambda$ do not change under these transformations. Using all these relations, we find that

$$f^{(\pm)}(k) = f^{(\mp)}(-k) = [f^{(\mp)}(k^\star)]^\star = [f^{(\pm)}(-k^\star)]^\star,$$

and

$$S(k) = \frac{1}{S(-k)} = \frac{1}{[S(k^\star)]^\star} = [S(-k^\star)]^\star. \quad (37)$$

The transformation $k \to -k^\star$ is the reflection relative to the imaginary k axis and is known as the mirror symmetry.

In the case (∗∗∗), i.e., when the tail of the potential is $\sim 1/r$, the analysis of the symmetry properties is a more complicated. In such a case the Jost functions are written as

$$f^{(\pm)}(k) = \cos(\lambda R)\mathcal{H}_{\eta,0}^{(\pm)}(kR) - \frac{\sin(\lambda R)}{\lambda}\mathcal{H}_{\eta,0}^{(\pm)\prime}(kR), \quad (38)$$

where the Coulomb functions $\mathcal{H}_{\eta,0}^{(\pm)}(kR)$ and their derivatives are not single-valued functions of the energy. They can be presented as the sums of the other functions which involve the multivalued and single-valued factors (see Appendix A). The symmetry properties can be established by analyzing how these factors change under the sign change and complex conjugation of the momentum.

For $\ell = 0$ the Coulomb functions can be written in the following factorized form:

$$\mathcal{H}_{\eta,0}^{(\pm)}(z) = \frac{\exp(\pi\eta/2)}{\Gamma(1 \pm i\eta)}[h_{\eta,0}^{(\pm)}\Phi_{\eta,1}(z) + \Psi_{\eta,1}(z)],$$

$$\frac{d}{dz}\mathcal{H}_{\eta,0}^{(\pm)}(z) = \frac{\eta\exp(\pi\eta/2)}{\Gamma(1 \pm i\eta)}[h_{\eta,0}^{(\pm)}\tilde{\Phi}_\eta(z) + \tilde{\Psi}_\eta(z)],$$

where for $z = kR$ the functions $\Phi_{\eta,1}(z)$, $\Psi_{\eta,1}(z)$, $\tilde{\Phi}_\eta(z)$, and $\tilde{\Psi}_\eta(z)$ are single-valued functions of k^2 (i.e., of the energy). The multivaluedness of the Coulomb functions and therefore of the Jost functions (38) stems from the other factors. Since the Sommerfeld parameter depends on the first power of the momentum, there is the square-root branch point of the Riemann surface at $E = 0$. An additional trouble is caused by the functions

$$h_{\eta,0}^{(\pm)} = \frac{1}{2}[\psi(i\eta) + \psi(-i\eta)] - \ln\eta \pm \frac{i\pi}{\exp(2\pi\eta) - 1},$$

making $E = 0$ also the logarithm branch point.

Substituting the factorized representations of the Coulomb functions in Eq. (38), we obtain

$$f^{(\pm)}(k) = \frac{\exp(\pi\eta/2)}{\Gamma(1 \pm i\eta)}[h_{\eta,0}^{(\pm)}\Theta(k^2) + \Sigma(k^2)],$$

where

$$\Theta(k^2) = \cos(\lambda R)\Phi_{\eta,1}(z) - \left(\frac{R}{a}\right)\frac{\sin(\lambda R)}{\lambda R}\tilde{\Phi}_\eta(z),$$

$$\Sigma(k^2) = \cos(\lambda R)\Psi_{\eta,1}(z) - \left(\frac{R}{a}\right)\frac{\sin(\lambda R)}{\lambda R}\tilde{\Psi}_\eta(z),$$

are entire (analytic and single-valued) functions of k^2. It is not difficult to see that, in contrast to the cases (∗) and (∗∗), the transformation $k \to -k$ does not lead to a simple relation between the Jost functions at these two points. Indeed, such a transformation changes η to $-\eta$ and thus $\exp(\pi\eta/2) \to \exp(-\pi\eta/2)$. Moreover, the functions $h_{-\eta,0}^{(\pm)}$ and $h_{\eta,0}^{(\pm)}$ have different values. This means that the presence of the Coulomb forces destroys the symmetry between the points k and $-k$ as well as the mirror symmetry, i.e., the symmetry between k and $-k^*$. The only symmetry that remains valid is the symmetry between the points k and k^*. A detailed discussion of the symmetry properties of the Jost matrices for multichannel problems can be found in Ref. [1], where the same results are obtained within a different (general) approach.

III. MIGRATION OF THE SPECTRAL POINTS

Having obtained the exact analytic expressions for the Jost matrices, we can locate zeros of $\det\hat{f}^{(+)}(k)$ and study how they move when the strength of the potential is changing. These zeros correspond to the poles of the S matrix, i.e., to the spectral points (bound, virtual, and resonant states) of the Hamiltonian. The method that we use for locating these spectral points is described in Appendix B.

In the models that we consider, the positions of the spectral points are determined by the following dimensionless parameters: kR, $R\sqrt{|V_i|}$, and ΔR^2. The idea of tracing the movement of the spectral points with the change of such parameters is taken from Ref. [12]. We did all the calculations with $R = 3$ fm (which is typical size of the potentials in nuclear physics). If necessary, all the results can be scaled to a different R. When varying the strength of the potential, we only change the flat potential at $r < R$, while the height of the external barrier is fixed.

A. Single-channel problem (∗)

To begin with, we consider the simplest case (∗) of the potential (33). The trajectories of the spectral points for an attractive well ($V_1 < 0$) are shown in Figs. 2(a) and 2(b), and for a repulsive barrier ($V_1 > 0$) in Fig. 2(c). These curves are the paths of the Jost function zeros when the potential strength, determined by the dimensionless parameter $R\sqrt{|V_1|}$, is changed. There are few points shown on each trajectory with the numbers next to them indicating the corresponding values of this parameter.

The first obvious feature in these figures is the mirror symmetry of the zeros [see Figs. 2(b) and 2(c)]. They appear in pairs on both sides of the imaginary axis at k and $-k^*$. There are infinitely many of them. When $V_1 = 0$, all the zeros are at infinity in the lower half of the k plane. When the bottom, V_1, of the potential well moves down, the zeros become visible and migrate towards the point $kR = -i$. At this point the left
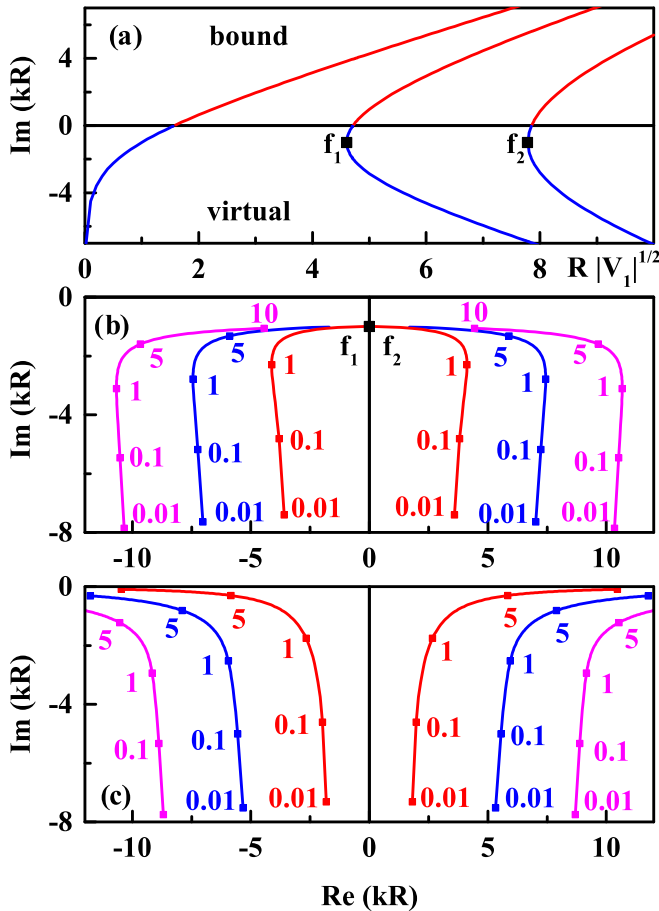
FIG. 2. Trajectories of the Jost function zeros for the single-channel square-well potential with variable depth in the internal region and zero potential outside: (a) migration of the first three zeros along the imaginary axis kR as a function of the dimensionless strength parameter $R\sqrt{|V_1|}$; (b) movement of the zeros on the complex plane kR. Both cases (a) and (b) are for an attractive well $V_1 < 0$. (c) The trajectories of the zeros on the complex kR plane for a repulsive barrier $V_1 > 0$. The numbers show the values of the parameter $R\sqrt{|V_1|}$ at the corresponding points of the trajectories.
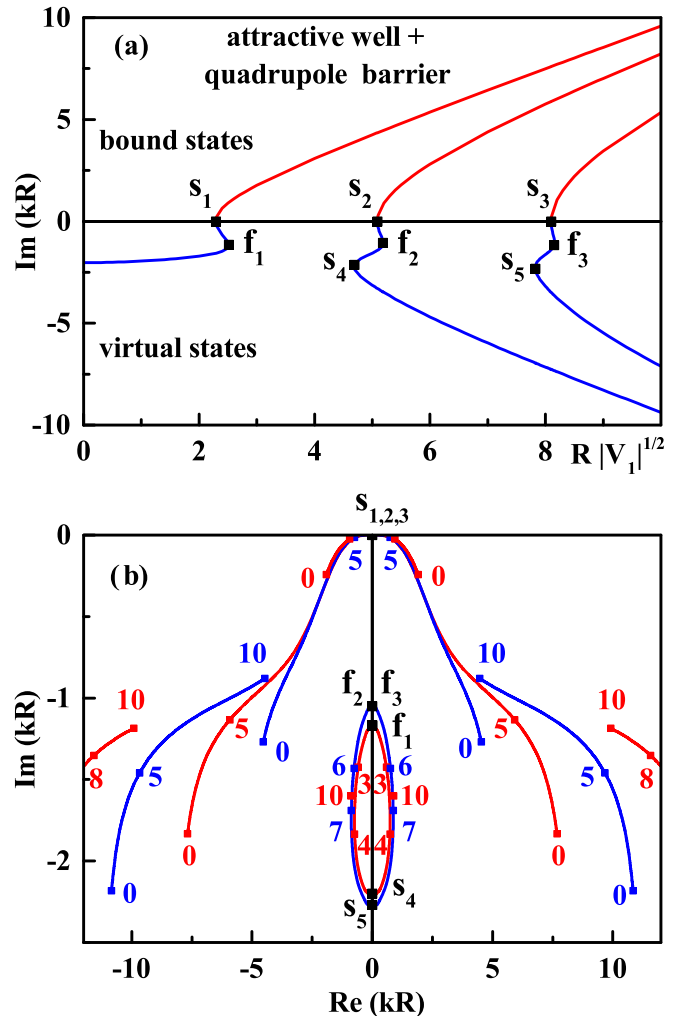

FIG. 3. Trajectories of the Jost function zeros for the attractive square well potential with the quadrupole centrifugal barrier in the external region: (a) movement of the poles along the imaginary kR axis with the change of the dimensionless strength parameter $R\sqrt{|V_1|}$; (b) movement on the complex kR plane. Numbers at the points of the trajectories in panel (b) give the values of the parameter $R\sqrt{|V_1|}$.

and right symmetric zeros fuse. The fusions of the first two pairs are marked by the symbols f_1 and f_2 in Figs. 2(a) and 2(b). After the fusion, they move along the imaginary axis in the opposite directions. The zero that moves down eventually disappears. Its partner that moves up becomes a bound state after crossing the threshold point $k = 0$. Further deepening of the potential moves this zero up along the imaginary axis and a new pair of zeros fuses at $kR = -i$.

For the attractive well, different symmetric pairs of the zeros fuse at the same point, $kR = -i$, but at different depths of the potential, and repeat the same movement-pattern. There is, however, one zero that appears alone. It goes all the way from $-i\infty$ up along the imaginary axis and moves faster than the other zeros. After crossing the threshold, it becomes the ground bound state. In Fig. 2(a) its movement is represented by the leftmost curve. The other two trajectories in this figure show how the first two fusing pairs move from the points f_1

and f_2 in the opposite directions after they get to the imaginary axis [their preceding "history" is shown in Fig. 2(b)].

For a repulsive barrier ($V_1 > 0$), there are no zeros on the imaginary axis [see Fig. 2(c)]. In this case, symmetric pairs of the zeros move away from each other.

The pattern of the S-matrix pole migration, shown in Fig. 2, is typical for the short-range potentials. A similar picture of the S wave pole movement was reported, for example, for the Woods-Saxon potential in Ref. [13].

B. Single-channel problem (∗∗)

Figures 3(a) and 3(b) show the movement of the zeros for the attractive square-well potential (33∗∗) with variable depth and with fixed quadrupole centrifugal barrier outside. The notation is similar to Fig. 2.

Since even for $|V_1| = 0$ the fixed centrifugal barrier $6/r^2$ is present in the external region, the initial positions of the

spectral points (marked by 0) are not at infinity. They just form a typical sequence of resonances with the mirror symmetry relative to the imaginary axis [Fig. 3(b)] and one virtual state is visible on the imaginary k axis [Fig. 3(a)]. The movement of the zeros with increasing depth $|V_1|$ is also qualitatively different from the corresponding behavior of the poles in the case (∗) of a finite-range potential.

There are two different types of trajectories:

(i) The trajectories of the first type exhibit a similar pattern of movement as in the case (∗), namely, the symmetric zeros move towards each other and fuse. The difference is that they fuse not at the point $kR = -i$, but at the threshold $k = 0$. Similar to the case (∗), zeros at the fusion point (marked as s_1, s_2, and s_3) turn in 90° and start moving along the imaginary axis in opposite directions.

(ii) The trajectories of the second type are closed ellipses shown in the central part of Fig. 3(b). Initially, i.e., when $|V_1| = 0$, there is nothing there except for one virtual state. These ellipses are formed with growing $|V_1|$ by those virtual states that move down the imaginary axis from the first type of trajectories. These virtual states collide on the imaginary axis with the other virtual states that go up, and start moving sidewise symmetrically in the complex plane along the closed elliptic paths, repeating the collisions (trajectories that go down from the point f_3, overlap with those starting from the point f_2; this is why only the endpoints of these curves at $R\sqrt{|V_1|} = 10$ are shown).

Figure 4 shows how the zeros move when in the internal region, $r \leqslant R$, the square potential is repulsive with the quadrupole centrifugal tail outside. In the absence of the internal potential, $|V_1| = 0$, the initial distribution of the spectral points is, of course, the same as in the previous case (the points marked by zero in Fig. 4 and one virtual state). With increasing $|V_1|$ the resonances move away from the imaginary axis. Their trajectories do zigzags when the height of the internal barrier becomes equal to the height of the external one. The virtual state moves down the imaginary axis and collides (at the point f) with another virtual state which comes up from afar. After the collision they symmetrically move up in complex plane along the elliptic trajectories.

C. Single-channel problem (∗ ∗ ∗)

The height of the Coulomb barrier at $r = R$ in the single-channel potential (33∗ ∗ ∗) is chosen to be equal to the height of the quadrupole barrier that is used in the previous case, namely, $6/R^2$. It fixes the Bohr radius to $a = 1$ fm. Due to the presence of the logarithmic branch point, we have here infinite number of Riemann sheets. Among them, we only consider the two principal sheets, i.e., with the logarithmic index $m = 0$ and positive and negative Im k.

Figures 5 and 6 show the movements of the Jost function zeros with change of the flat potential V_1 down or up for the attractive or repulsive internal potential, respectively. The most important feature of these curves is that, in contrast to the previous cases, they are not symmetric relative to the
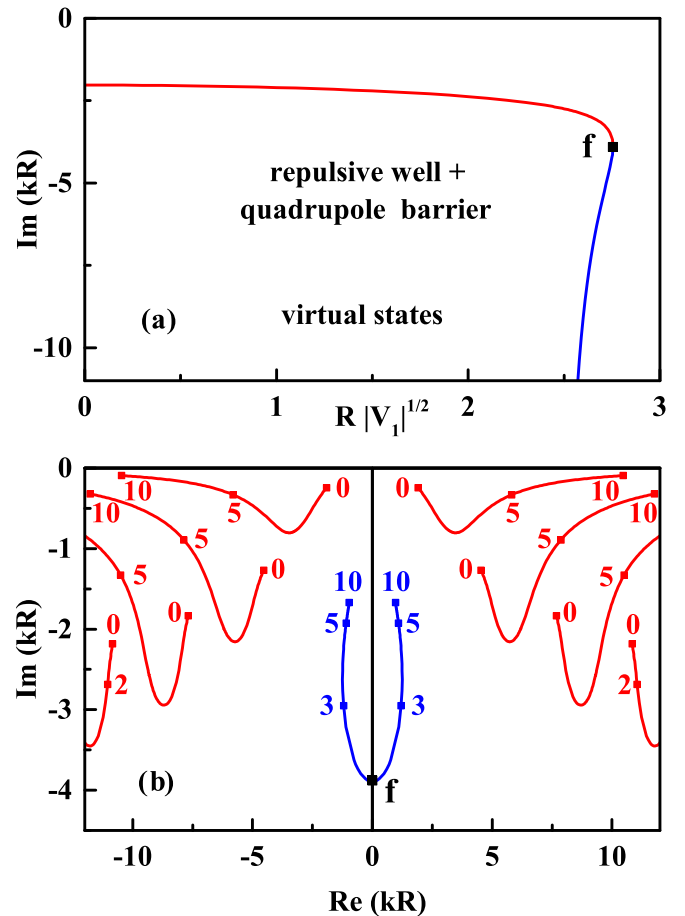

FIG. 4. Trajectories of the Jost function zeros for the repulsive square potential (33∗∗) with variable height and with fixed quadrupole centrifugal barrier outside. The notation is the same as for Fig. 2.

imaginary axis. This means that (as seen from the analytic expressions obtained in Sec. II C) the mirror symmetry is broken by the presence of the Coulomb forces.

Similarly to the case (∗∗), the resonance poles on the right of the imaginary axis move towards the threshold, where they change direction by 90° and continue to move up the imaginary axis as the bound states. However, in contrast with the case (∗∗), they do not collide at $k = 0$ with their partners on the left of the imaginary axis. These "left-hand" poles move differently. They approach the real axis from below, move along it towards the threshold, where they turn down by 90°, and continue to move down along the imaginary axis at a small distance from it. This pole motion is similar to one of the virtual states but it is not the case since the pole has a small but finite value of Re $k < 0$. Thus in this case the virtual states are absent.

To the right of the imaginary axis there is also a sequence of resonance poles that never become bound states. As shown in Fig. 5(b) and magnified in Fig. 5(c), these poles make a kind of "curls" and practically stay at their original places. These poles condense near the threshold, similarly to bound states of a hydrogen-like atom. The distribution pattern of these poles
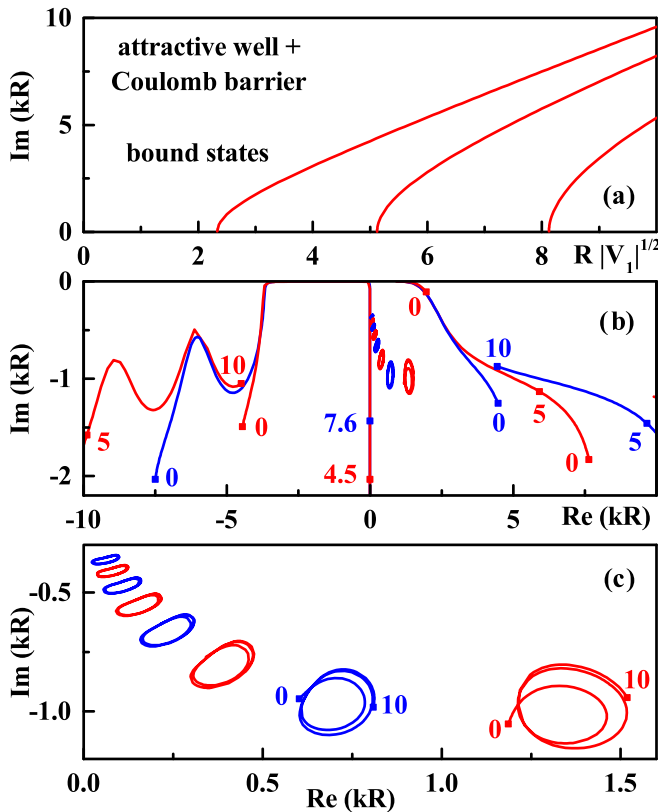
FIG. 5. Trajectories of the Jost function zeros for the attractive square well potential with different depths and the Coulomb barrier outside: (a) along the imaginary axis k as a function of the dimensionless strength parameter $R\sqrt{|V_1|}$; (b) in the complex plane k; (c) the larger scale fragment for some of the trajectories near the imaginary axis. The numbers near the symbols on the trajectories show the dimensionless strength parameter $R\sqrt{|V_1|}$.

FIG. 6. (a) Trajectories of the Jost function zeros in the complex k plane for the repulsive rectangular potential with different strengths and the Coulomb barrier outside. (b) The larger scale fragment for some of the trajectories near the imaginary axis. The numbers near the symbols on the trajectories indicate the dimensionless strength parameter $R\sqrt{|V_1|}$.

is similar to the pattern of zeros of the function $h_{\eta,0}^{(+)}$ (see, for example, the phase portrait of $h_{\eta,0}^{(+)}$ in Ref. [14]).

In the case of $V_1 > 0$ (repulsive rectangular potential) the behavior of the poles is basically the same as for the repulsive case (**). The main difference is that the Coulomb tail breaks down the mirror symmetry and generates the sequence of "curled" resonances condensing at the threshold. One more unusual feature here is that one of the poles moves up parallel and very close to the negative imaginary axis (a bit to the left of it) and almost at the threshold turns to the left. The motion of this pole is similar to the one discussed above for the attractive potential but with reverse direction of the movement.

In general, all these results clearly demonstrate a very strong influence of the potential behavior at large distances on the pattern of the spectral points and on their movements with the change of the potential strength. This also emphasizes the importance of using proper topology of the Riemann surface when studying the S-matrix singularities.

D. Parameters of the two-channel problem

In the two-channel case the distribution of the poles depends on the two diagonal potentials, on the coupling between
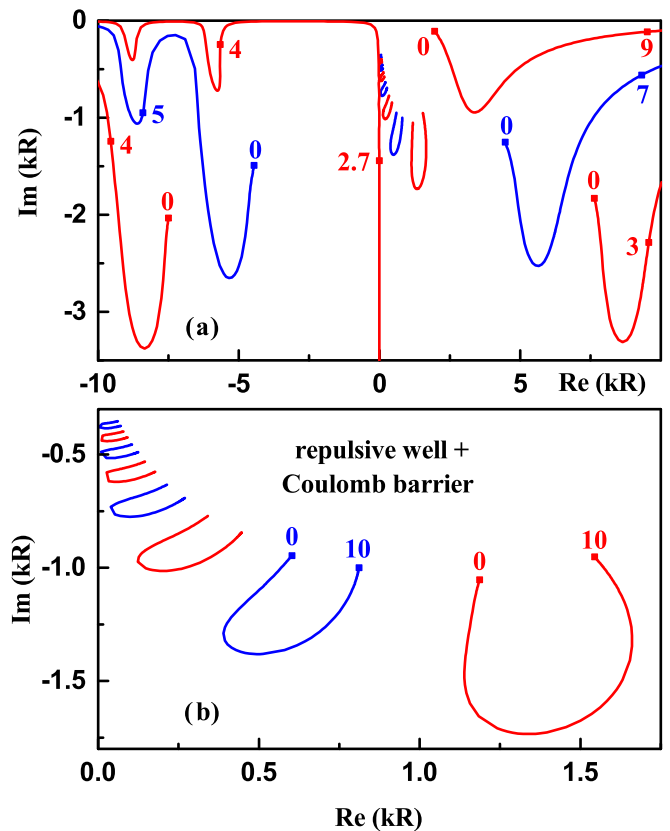
the channels, and on the threshold energy of the second channel (because $E_1 = 0$). Therefore there are many possible parameters and their combinations that can be varied in studying the migration of the poles. To narrow the choices, we use the same three models, (*), (**), and (***), for the diagonal potentials and only vary the coupling between the channels, which in our calculations is represented by the dimensionless parameter $R\sqrt{\Delta}$, where $\Delta = V_{1,2}(r) = V_{2,1}(r)$ is a constant potential term that couples the channels. The physical meaning of the parameter $R\sqrt{\Delta}$ is the same as for the product kR. Indeed, defined by Eq. (1), the reduced potential V is measured in the units of inverse square of the length. Therefore, $\sqrt{\Delta}$ is the wave number that corresponds to the coupling potential.

In all the cases considered below, we choose the dimensionless threshold to be $\varepsilon_2 R^2 = 4.306$ (with $R = 3$ fm this corresponds to $\varepsilon_2 = 10$ MeV). The heights of the centrifugal and Coulomb potentials at $r = R$ are chosen to be the same as in the preceding sections.

The sheets of the Riemann energy surface are marked by the signs of the imaginary parts of the channel momenta. For example, the symbol $(+, -)$ labels the sheet with (Im $k_1 > 0$, Im $k_2 < 0$). When the Coulomb tail is present in one of the
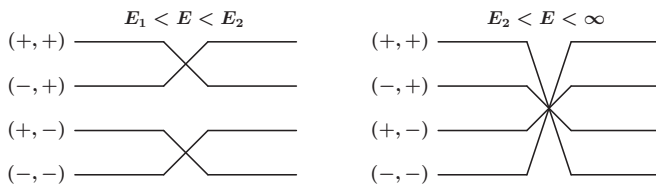
FIG. 7. Interconnections of the Riemann sheets in the two-channel problem with a short-range potential.

two channels, the symbol denoting a Riemann sheet, involves the logarithmic index m, such as, for example, $(+, -)_m$. If the Coulomb tails are in both channels, the two indexes m_1 and m_2 appear.

Each of the Riemann sheets has its own real axis with its origin at the threshold energy and is cut along it from 0 to $+\infty$. The edges of the cuts of different sheets are interconnected. In the absence of the Coulomb forces there are just four sheets. When the potential has a Coulomb tail at least in one of the channels, the number of the sheets becomes infinite and their interconnections provide the spiral topology of the Riemann surface. The interconnections are different in the interval between the thresholds and from the second threshold to infinity. Such interconnections are schematically shown in Fig. 7 for the neutral particles. Figure 8 shows interconnections for the case where the Coulomb interaction is in the first channel and absent in the second. These drawings should be understood as the cross sections of the Riemann surfaces, perpendicular to the real axes. In the case of the potential with a Coulomb tail, we are only interested in the principal sheets $(+, +)_0$, $(-, +)_0$, $(+, -)_0$, and $(-, -)_0$, which are shown in Fig. 8 by the thick lines. Pseudo three-dimensional (3D) images of this surface can be found in Refs. [1,9], where it is explained why the interconnections are done in this way.

E. Two-channel problem (∗)

1. Shallow square wells

Figure 9 shows the trajectories of the S matrix poles on different sheets of the Riemann surface of the energy [$E \sim$
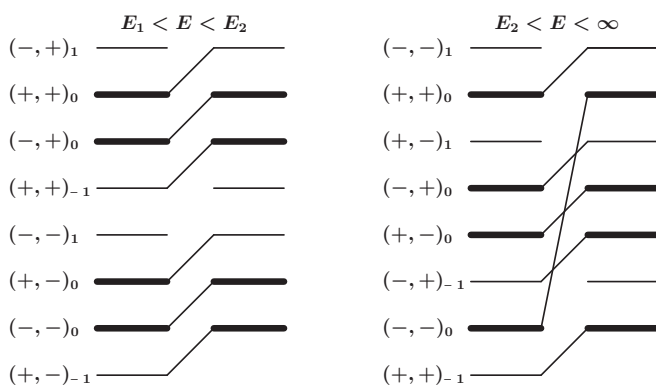

FIG. 8. Interconnections of the Riemann sheets in the two-channel problem with a short-range plus Coulomb potential. The principal sheets are shown by the thick lines.

$(kR)^2$] as the functions of the coupling-strength ($c = R\Delta^{1/2}$) between the two channels. The diagonal potentials are the attractive square wells ($R\sqrt{|V_{11}|} = R\sqrt{|V_{22}|} = 0.5678$) of the same radius R. For $r > R$ the potential is identically zero in both channels. The diagonal potentials are shallow and do not support any bound states. With $c = 0$ there are no poles on the physical sheet $(+, +)$.

When the coupling between the channels grows, some of the poles move from the other sheets to the physical one by crossing the threshold point $E = 0$. It is the only point through which the poles appear on the physical sheet. With further increase of c these poles remain on the negative real axis of the physical sheet $(+, +)$, where they correspond to the bound states. No other poles on the physical sheet are found.

As seen in Figs. 9(b)–9(d), there is the mirror symmetry of the poles on all the nonphysical sheets. On these sheets they always appear in symmetric pairs. Symmetric pairs can fuse at one point at negative real energies (points marked by the symbols f_1, f_2, and f_3 in Fig. 9). With increasing coupling they split and continue to move along the real axis at negative energies in different directions: one to $-\infty$ and the other pole to zero. These movements are shown in Fig. 9(a), where the negative energy is represented on the vertical axis by pure imaginary $k \sim \sqrt{E}$. The pole which crosses the zero, continues to move on another energy sheet along the negative real axis. Two symmetric poles can also meet each other at the real positive energies [the points $s^{(\pm)}$ in Figs. 9(c) and 9(d)], where the sheet has the cut. Since they come to this point from different sides of the cut, they cannot fuse. Instead, they transit via these points to the other unphysical sheets.

Figure 9(a) shows that only those poles that previously were resonances can become the bound states. Indeed, the resonance poles are located on the Riemann sheets where the channel momenta have positive imaginary parts for all open channels. If two channels are open, then the resonances are on the sheet $(-, -)$ with the wave functions that have growing asymptotic behavior in both channels. If one channel is open, the resonances are on the sheet $(-, +)$ where the wave function in the closed channel is exponentially vanishing at large distances. In our case, at low energies (near $E = 0$) the second channel is closed and the resonances are on the sheet $(-, +)$, which is nonphysical with respect to the first channel and physical with respect to the second one. And we see that only from the fusion points f_1 and f_3 [which are on the sheet $(-, +)$] do the poles come to the sheet $(+, +)$ and turn into bound states. At the same time, from point f_2, where a subthreshold resonance fuses with its mirror partner, the pole moves to the nonphysical sheet $(+, -)$.

2. Deep square wells

The next example that we consider only differs from the previous one by the depths of the square wells. We chose them to be $R\sqrt{|V_{11}|} = R\sqrt{|V_{22}|} = 3$. With such a choice there are two bound states even when there is no coupling between the channels. This is seen in Fig. 10(a), where there are two trajectories starting at $\Delta = 0$ from positive (pure) imaginary $kR \sim \sqrt{E}$. When the coupling is increasing, one bound state becomes more strongly bound while the other moves in the
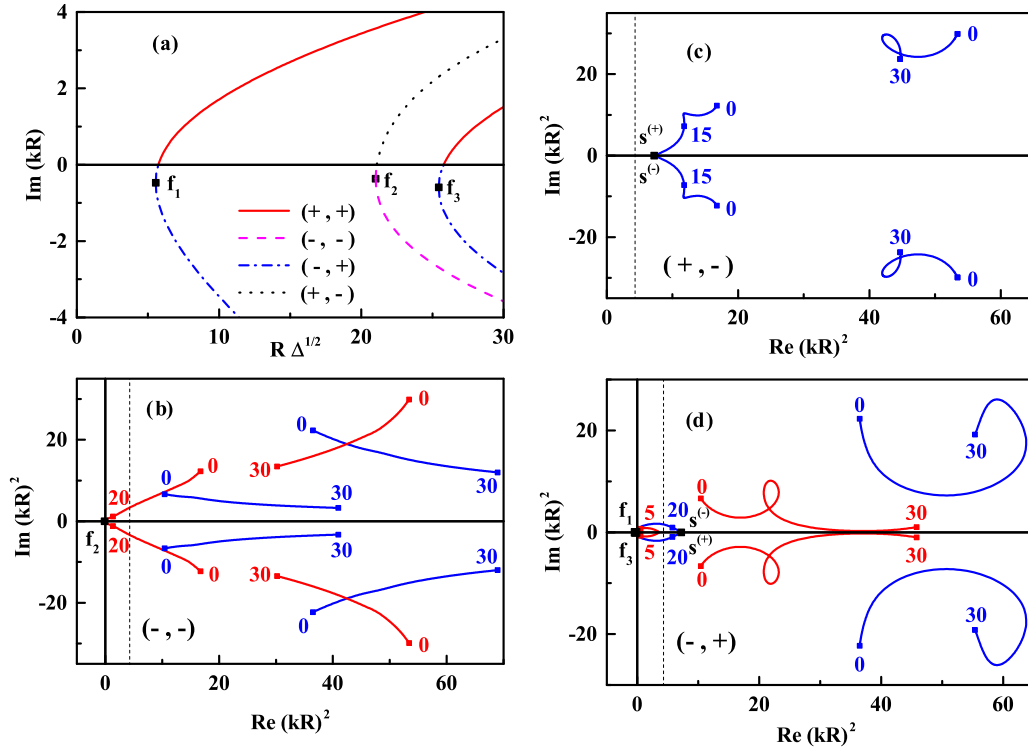
FIG. 9. Trajectories of the S-matrix poles on different energy sheets $(\pm, \pm)$ for two coupled shallow square wells of the radius R with zero potential beyond this radius. Without the coupling these square wells do not support any bound states. The curves are presented in the dimensionless coordinates: momentum $kR \sim \sqrt{E}$, energy $(kR)^2 \sim E$, and the coupling strength $R\sqrt{\Delta}$. Vertical dashed line at $(kR)^2 = 4.306$ indicates the position of the second threshold.

opposite direction, i.e., becomes less bound. Then, after crossing the zero energy, it moves from the physical sheet to the sheet $(-, +)$ where it becomes a virtual state.

Despite the seemingly slight difference of this (deep) two-channel potential from the previous (shallow) one, the pattern of the pole-trajectories turned out to be significantly different, as seen in Figs. 10(a)–10(c). However, still there are no complex poles on the physical sheet $(+, +)$ and all trajectories are mirror symmetric. The only route to the physical sheet is via the zero energy point and at the positive energies it is possible to move across the cuts only between the nonphysical sheets [points $s^{(\pm)}$ in Figs. 10(c) and 10(d)].

F. Two-channel problem (∗∗)

Now we add the external centrifugal barrier (with $\ell = 2$) to the deep square-well potential of Sec. III E 2. Here we consider the two cases: when the centrifugal barrier is added to either the first or to the second channel. The corresponding pole-trajectories are presented in Figs. 11 and 12, respectively. The patterns of the pole migration in these cases are rather different. There is, however, a common and most remarkable feature in these figures, namely, the appearance of complex S-matrix poles on the *physical* sheet $(+, +)$, which in the two-channel problem is a consequence of the addition of the long-range tail ($\sim 1/r^2$) in the external region.

In Figs. 11 and 12 the points where the trajectories reach the cuts from different sides are denoted by the symbols $s^{(\pm)}$

and $s^{(\pm)}_{1,2}$. Although they are depicted at the same place, the points $s^{(+)}$ and $s^{(-)}$ do not coincide because the upper and lower edges of the cut are connected to different Riemann sheets. The corresponding points on the connected sheets are those from which the trajectories are continued. As is seen, in contrast with all the problems that we considered so far, here the transitions from one sheet to another happens not only via the thresholds but also by crossing the cuts.

Since in the model (∗∗) there is no Coulomb potential, the mirror symmetry of the poles is preserved. At some points marked by the symbols f_1, f_2, f_3, f_4 the symmetric pairs of the poles fuse. After the fusion (with further increase of the channel coupling) these poles split again and continue to move either along the negative real energy axis in the opposite directions or symmetrically into the complex domains. A more detailed picture of their movement along the negative real axes (on different sheets) is shown in Figs. 13(a) and 13(b) for the cases when the external $\sim r^{-2}$ tail is added to the first second channel, respectively.

G. Two-channel problem (∗∗) + (∗∗∗)

Finally, we consider the problem where both the centrifugal and Coulomb tails are present. In the internal region ($r \leqslant R$) the potential is the same as in the previous section, i.e., the deep square wells ($R\sqrt{|V_{11}|} = R\sqrt{|V_{22}|} = 3$). In the external region the Coulomb potential is in the first channel and the centrifugal barrier is in the second channel. Figure 14
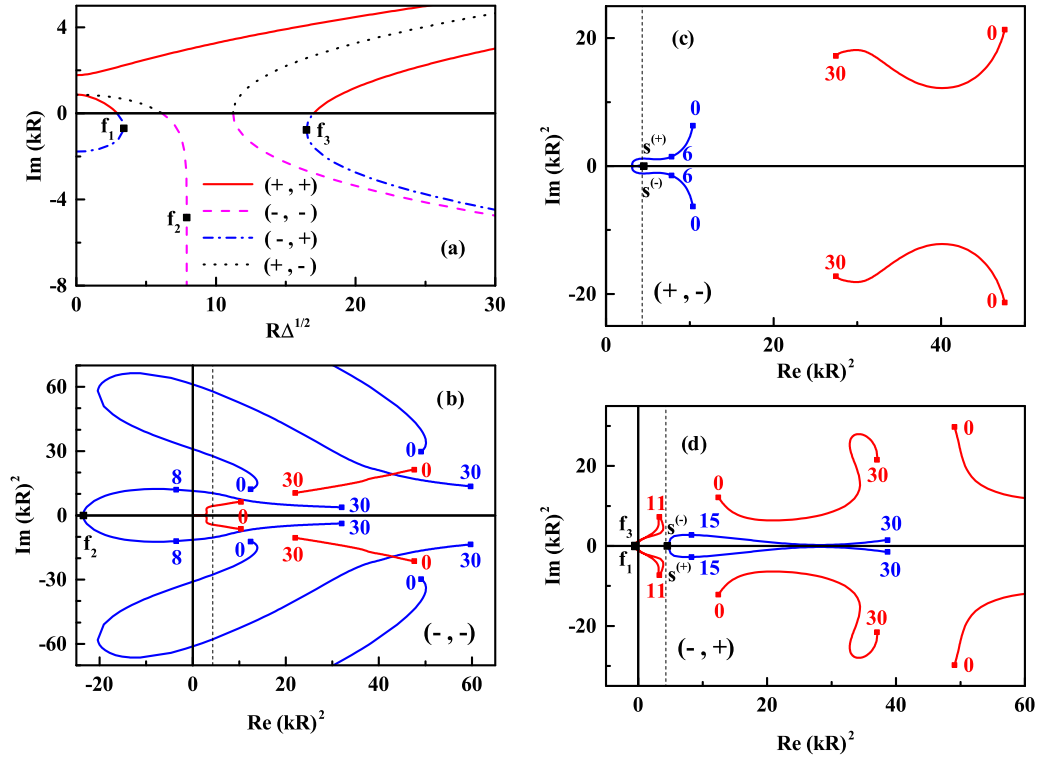
FIG. 10. Trajectories of the S-matrix poles on different energy sheets $(\pm, \pm)$ for two coupled deep square wells of the radius R with zero potential beyond this radius. Even without the coupling these square wells support two bound states. The curves are presented in the dimensionless coordinates: momentum $kR \sim \sqrt{E}$, energy $(kR)^2 \sim E$, and the coupling strength $R\sqrt{\Delta}$. Vertical dashed line at $(kR)^2 = 4.306$ indicates the position of the second threshold.
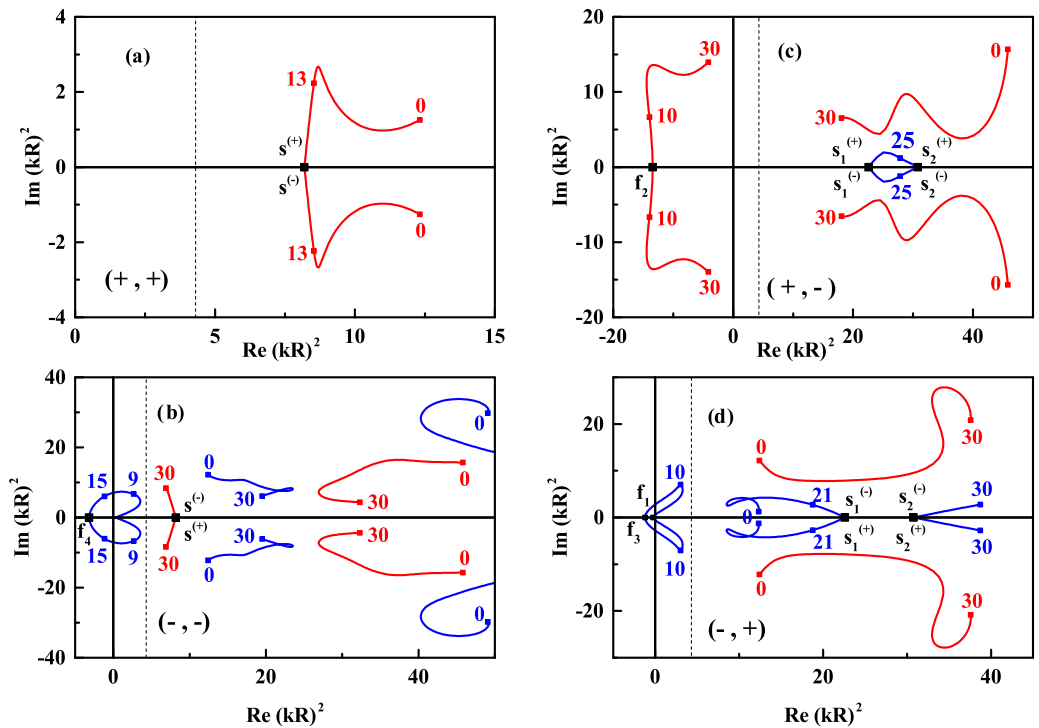

FIG. 11. Trajectories of the S-matrix poles on different energy sheets $(\pm, \pm)$ for two coupled square-wells of the radius R. Beyond this radius the potential is zero in the first channel and has the centrifugal tail $(6/r^2)$ in the second channel. The vertical dashed line at $(kR)^2 = 4.306$ indicates the position of the second threshold.
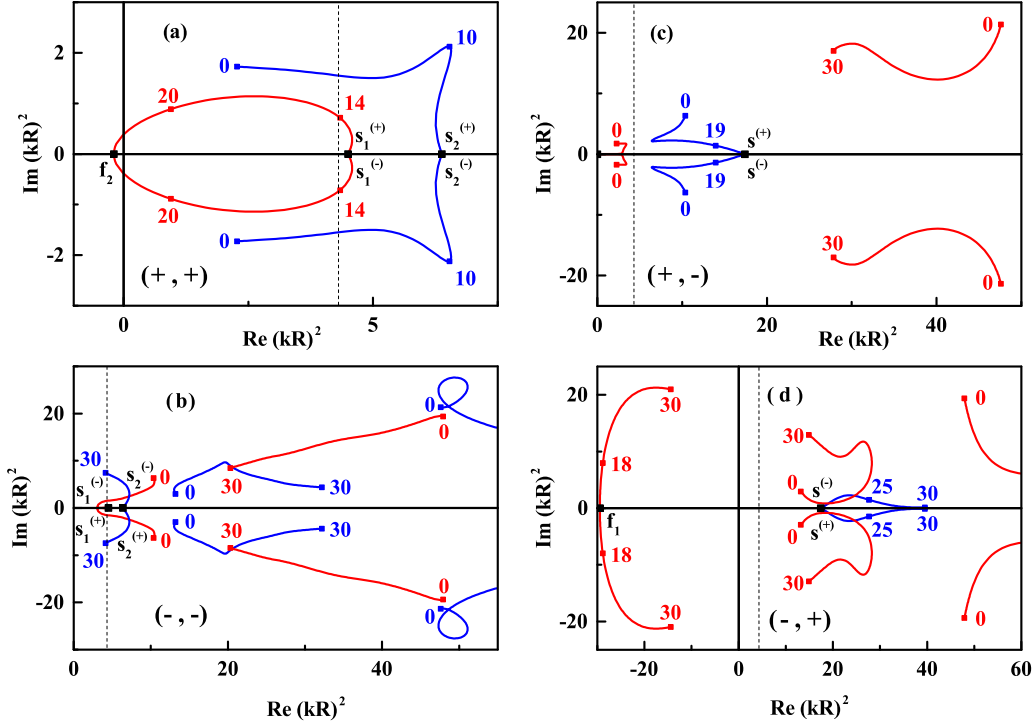
FIG. 12. Trajectories of the S-matrix poles on different energy sheets $(\pm, \pm)$ for two coupled square wells of radius R. Beyond this radius the potential has the centrifugal tail $(6/r^2)$ in the first channel and is zero in the second channel. Vertical dashed line at $(kR)^2 = 4.306$ indicates the position of the second threshold.

shows the migration of the S-matrix poles on the principal Riemann sheets and in Fig. 15 their movements along the real negative-energy axes on different sheets are shown. Since it is not possible to distinguish the trajectories along the same line, the movements along the real negative-E axes are given in Fig. 15 in the coordinates kR versus $R\sqrt{\Delta}$, where the pure imaginary $k \sim \sqrt{E}$ represents the corresponding energy.

Looking at Figs. 15(b), 15(d), 15(e), and 15(f), we first of all see that the mirror symmetry is broken as was expected from the analysis of the explicit solutions in Sec. II. The second important feature [the same as in the case $(**)$] is that there are poles at complex energies on the physical sheet $(+, +)$.

The meaning of the symbols used here is the same as in the previous figures. In particular, f denotes the fusion point, and $s^{(\pm)}$, $s_{1,2}^{(\pm)}$ are the points where the poles cross the branch cut approaching from different sides. Since the Coulomb forces change the topology of the Riemann surface and destroy mirror symmetry, some trajectories after crossing the cuts leave the principal sheets with $m = 0$ and continue to nonprincipal sheets with $m \neq 0$ or can appear on a principal sheet from the sheets with $m \neq 0$. When trajectories move to nonprincipal sheets, we do not trace them beyond these points. Examples of such trajectories are those whose endpoints are $s^{(-)}$ in Fig. 15(a) and $s_{1,2}^{(-)}$ in Fig. 15(c).

IV. CONCLUSIONS

Using the exactly solvable one- and two-channel models, it is shown how the S-matrix poles are distributed over the

Riemann surface of the energy and how they migrate when the parameters of the interaction are changed. The following two facts that are observed in this study should be noted:

(i) The Coulomb forces break down the mirror symmetry of the S-matrix poles.

(ii) In the multichannel problems with long-range interactions the S-matrix poles may appear on the physical sheet of the Riemann surface at complex energies.

In nuclear and atomic physics we mostly deal with charged particles and therefore the first of these two facts has to be taken into account not only in a theoretical description of such physical systems but also in the analysis of experimental data. This is especially important when constructing certain phenomenological models and developing approximate methods, where the patterns of the pole-distribution are pre-assumed.

The second fact (i.e., the possibility of the seemingly "forbidden" poles appearing on the physical sheet) should be kept in mind when the channels have different orbital angular momenta. In such a case the increase of the centrifugal barrier in one of the channels can be treated as an additional long-range ($\sim 1/r^2$) potential that may generate such poles. In other words, if the channels have different ℓ, then the possibility of finding such forbidden poles cannot be excluded.

Although the models used in the present study are rather simple, they more or less correspond to actual interactions that we usually deal with in nuclear physics. Our main task was to demonstrate the above two facts in an explicit way. This is why we only analyzed the states with $\ell = 0$, where all the formulas are transparent and clear. In principle, the same
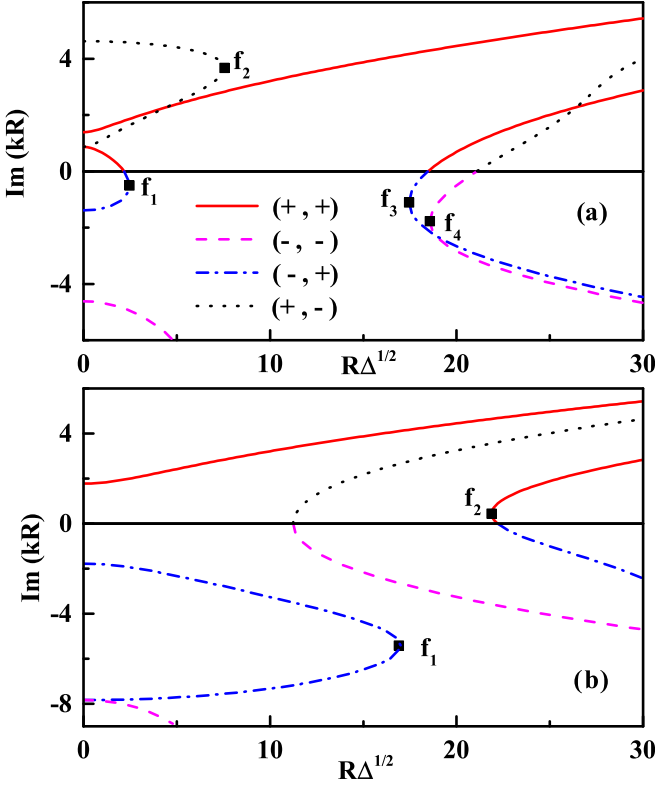
FIG. 13. Migration of the S-matrix poles along the real negative-energy axes on different Riemann sheets. The negative energy is represented by pure imaginary $k \sim \sqrt{E}$. Panels (a) and (b) correspond to zero external potential in the first and second channels, respectively. In both cases there is the quadrupole centrifugal potential in the other channel.

approach based on subdivision of the configuration space in the internal and external regions and constructing the Jost matrices can be used for treating some more complicated problems. One can obtain an exact analytic solution of such a problem if it is possible to analytically solve it in both regions.

APPENDIX A: COULOMB FUNCTIONS

The properties and analytic structure of the Coulomb wave functions are very complicated but well studied (see, for example, Ref. [14] and references therein). The standard regular and irregular Coulomb functions, $F_{\eta,\ell}(z)$ and $G_{\eta,\ell}(z)$, as well as their linear combinations $H_{\eta,\ell}^{(\pm)} = G_{\eta,\ell} \pm iF_{\eta,\ell}$ (that describe the Coulomb spherical waves), are multivalued functions of the complex variable z. They are defined on a Riemann surface with the branch point at $z = 0$ and a cut along the negative real axis. In quantum-mechanical problems these functions are used with $z = kr$, where k and r are the wave number and the radial distance.

In the present work we use the Coulomb functions at real r and complex values of k. Our numerical calculations of them are based on the approach developed in Ref. [15], the central part of which is the expansion of the regular Whittaker function in the series of the Bessel functions, suggested in Ref. [16]. After some rearrangement, such series for the

functions $H_{\eta,\ell}^{(\pm)}(kr)$ can be written as

$$H_{\eta,\ell}^{(\pm)}(z) = \frac{(2\eta)^{\ell}}{C_{\eta,\ell}\Gamma(2\ell+2)}[\omega_{\eta,\ell}h_{\eta,\ell}^{(\pm)}\Phi_{\eta,\Lambda}(z) + \Psi_{\eta,\Lambda}(z)],$$

$$\Psi_{\eta,\Lambda} = \omega_{\eta,\ell}[\partial_{\nu}\Phi_{\eta,\nu}]_{\nu=\Lambda} + [\partial_{\nu}\Phi_{\eta,\nu}]_{\nu=-\Lambda}, \tag{A1}$$

where $\Lambda = 2\ell + 1$. The functions $\Phi_{\eta,\nu}(z)$ and $\partial_{\nu}\Phi_{\eta,\nu}(z)$ are entire functions of k^2. They can be expanded in the absolutely and uniformly convergent series:

$$\Phi_{\eta,\Lambda}(kr) = \sum_{m=0}^{\infty} \eta^{-2m}I_m^{(\Lambda)}(x), \tag{A2}$$

$$[\partial_{\nu}\Phi_{\eta,\nu}(kr)]_{\nu=\Lambda} = \sum_{m=0}^{\infty} \eta^{-2m}\dot{I}_m^{(\Lambda)}(x), \tag{A3}$$

where the functions $I_m^{(\Lambda)}$ and $\dot{I}_m^{(\Lambda)}$, depending on the real k-independent variable $x = \sqrt{8(r/a)}$ [with $a = \hbar^2/(\mu e^2 Z_1 Z_2)$ being the Bohr radius], for a repulsive Coulomb interaction are the following finite sums of the modified Bessel functions $I_{\nu}(x)$ and their derivatives $\partial_{\nu}I_{\nu}$ with respect to the order ν:

$$I_m^{(\Lambda)}(x) = (-1)^m \sum_{j=0}^{m} \left(\frac{x}{2}\right)^{2m+j+1} \beta_{m,j}^{(\Lambda)}I_{n+j}(x),$$

$$\dot{I}_m^{(\Lambda)}(x) = (-1)^m \sum_{j=0}^{m} \left(\frac{x}{2}\right)^{2m+j+1}$$

$$\times \left\{[\partial_{\nu}\beta_{m,j}^{(\nu)}]_{\nu=\Lambda}I_{n+j}(x) + \beta_{m,j}^{(\Lambda)}[\partial_{\nu}I_{\nu}(x)]_{\nu=n+j}\right\},$$

where $n = 2m + \Lambda$ and for the coefficients $\beta_{m,j}^{(\Lambda)}$ the following simple recurrency relations are available [15]:

$$\beta_{m,j}^{(\Lambda)} = \frac{\beta_{m-1,j-1}^{(\Lambda)}}{4(2m+j)} + \frac{(\Lambda+2m+j-1)}{4(2m+j)}\beta_{m-1,j}^{(\Lambda)},$$

$$\partial_{\nu}\beta_{m,j}^{(\nu)} = \frac{\partial_{\nu}\beta_{m-1,j-1}^{(\nu)}}{4(2m+j)} + \frac{(2m+j-1)}{4(2m+j)}\beta_{m-1,j}^{(\nu)}$$

$$+ \frac{(\nu+2m+j-1)}{4(2m+j)}\partial_{\nu}\beta_{m-1,j}^{(\nu)},$$

with the initial conditions $\partial_{\nu}\beta_{0,0}^{(\nu)} = 0$, $\beta_{0,0}^{(\Lambda)} = 1$, and the definition that $\beta_{m,j}^{(\Lambda)}$ as well as the derivative $\partial_{\nu}\beta_{m,j}^{(\nu)}$ are zero for $j < 0$ or $j > m$.

In the decompositions (A2) and (A3) the functions $I_m^{(\Lambda)}(x)$ and $\dot{I}_m^{(\Lambda)}(x)$ are rapidly decreasing with growth of the order m. The number of terms in these expansions that are needed for their numerical convergence depends on the energy.

The other factors in Eq. (A1) can be found as follows:

$$C_{\eta,\ell} = \frac{2^{\ell}[\Gamma(\ell+1+i\eta)\Gamma(\ell+1-i\eta)]^{1/2}}{\Gamma(2\ell+2)\exp(\pi\eta/2)},$$

$$\omega_{\eta,\ell} = \frac{\Gamma(\ell+1\pm i\eta)}{(\pm i)^{(2\ell+1)}\Gamma(-\ell\pm i\eta)} = \prod_{j=0}^{\ell}\left(1 + \frac{j^2}{\eta^2}\right),$$

$$h_{\eta,\ell}^{(\pm)} = \frac{1}{2}[\psi(\ell+1\pm i\eta) + \psi(-\ell\pm i\eta)] - \ln(\pm i\eta),$$

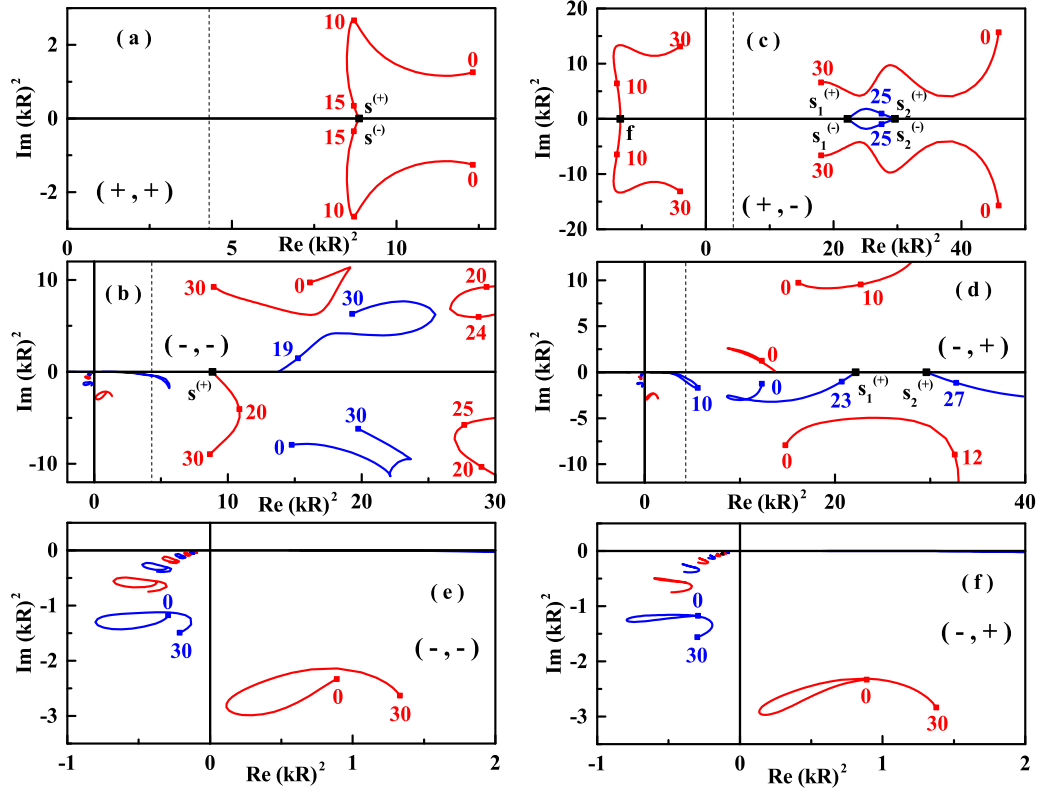$$\psi(z) = \Gamma(z)'/\Gamma(z). \tag{A4}$$

FIG. 14. Trajectories of the S-matrix poles on different energy sheets $(\pm, \pm)$ for two coupled square wells of radius R. Beyond this radius the potential has the Coulomb tail in the first channel and the centrifugal potential $(6/r^2)$ in the second channel. Vertical dashed line at $(kR)^2 = 4.306$ indicates the position of the second threshold.

The multivaluedness and singularities of $H_{\eta,\ell}^{(\pm)}(kr)$ in the complex-k plane originate from the factors $C_{\eta,\ell}$ and $h_{\eta,\ell}^{(\pm)}$. The
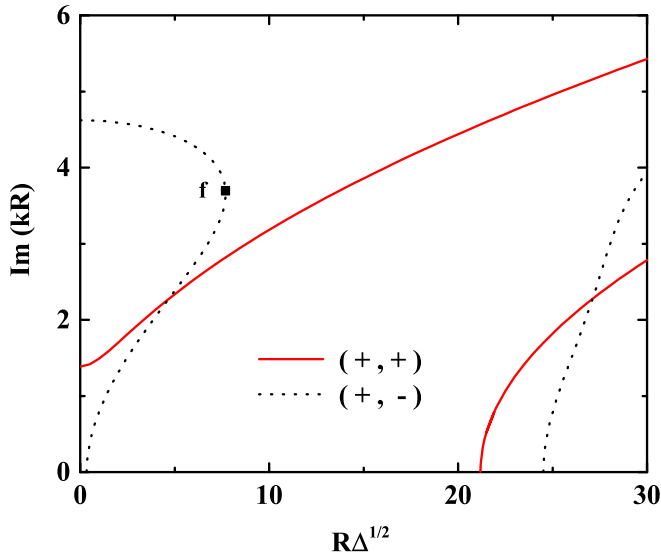

FIG. 15. Migration of the S-matrix poles along the real negative-energy axes on the two Riemann sheets. The negative energy is represented by pure imaginary $k \sim \sqrt{E}$. The potential is the same as for Fig. 14.

functions $h_{\eta,\ell}^{(\pm)}$ have the Coulomb poles accumulating at the origin where they also have the logarithmic branch point and the cut from $k = 0$ to $k = -\infty$.

For the functions

$$\mathcal{H}_{\eta,\ell}^{(\pm)}(z) = \exp\left(\mp i\sigma_{\eta,\ell}\right) H_{\eta,\ell}^{(\pm)}(z),$$

the common factor in the first of Eqs. (A1) is more simple,

$$\exp\left(\mp i\sigma_{\eta,\ell}\right) \frac{(2\eta)^\ell}{C_{\eta,\ell}\Gamma(2\ell+2)} = \frac{\eta^\ell \exp\left(\pi\eta/2\right)}{\Gamma(\ell+1\pm i\eta)}.$$

As a result, in the coefficients $h_{\eta,\ell}^{(\pm)}$ the poles of the digamma function $\psi(\ell+1\pm i\eta)$ at negative integer values of $(\ell+1\pm i\eta)$ are canceled with the corresponding poles of the function $\Gamma(\ell+1\pm i\eta)$ in the denominator, i.e.,

$$\psi(z)/\Gamma(z)\big|_{z=-n} = (-1)^{n+1}n!.$$

Therefore, in contrast with $H_{\eta,\ell}^{(\pm)}(kr)$, the Coulomb-distorted spherical waves $\mathcal{H}_{\eta,\ell}^{(\pm)}(kr)$ are well defined.

In numerical calculations, one has to use a consistent procedure for determining an appropriate number of $2\pi i$ in the complex logarithm when $\ln\Gamma(z)$ and $\psi(z)$ are evaluated. As such a procedure, we used the one suggested in Ref. [17]. The derivatives, $H_{\eta,\ell}^{(\pm)\prime}(z)$, of the Coulomb functions can be found

with the help of the recurrency relations [18]:

$$
\begin{aligned}
H_{\eta,\ell}^{(\pm)\prime}(z) = {} & \left(\frac{\ell+1}{z} + \frac{\eta}{\ell+1} \right) H_{\eta,\ell}^{(\pm)}(z) \\
& - \left[1 + \frac{\eta^2}{(\ell+1)^2} \right]^{1/2} H_{\eta,\ell+1}^{(\pm)}(z).
\end{aligned}
$$

APPENDIX B: LOCATING COMPLEX ZEROS

The S-matrix poles correspond to the zeros of the Jost matrix determinant. Instead of locating the poles, we therefore looked for the zeros. In doing this, we used the Cauchy's argument principle of complex analysis (see, for example, Ref. [19]) as well as the iterative Newton method for locating zeros of a complex function (see Ref. [20]).

For a meromorphic function $f(z)$ the argument principle relates a closed contour integral to the difference between the number of zeros and poles of that function enclosed by the contour,

$$
\frac{1}{2i\pi} \oint_C dz \frac{f'(z)}{f(z)} = N - P,
$$

where N and P are the numbers of the zeros and poles, respectively, with each zero and pole counted as many times as its multiplicity and order.

In the numerical calculations we used the contour of a rectangular shape. We knew for sure that our function could only have zeros. If the number of zeros inside the contour was greater than one, we subdivided the original contour into two halves and repeated the procedure until a sufficiently small domain was found with only one zero. After that we used Newton's method to refine the search.

[1] S. A. Rakityansky and S. N. Ershov, Int. J. Mod. Phys. E **28**, 1950064 (2019).

[2] N. G. van Kampen, Phys. Rev. **91**, 1267 (1953).

[3] R. E. Brown, N. Jarmie, and G. M. Hale, Phys. Rev. C **35**, 1999 (1987).

[4] G. M. Hale, R. E. Brown, and N. Jarmie, Phys. Rev. Lett. **59**, 763 (1987).

[5] B. M. Karnakov, V. D. Mur, S. G. Pozdnyakov, and V. S. Popov, JETP Lett. **51**, 399 (1990).

[6] L. N. Bogdanova, G. M. Hale, and V. E. Markushin, Phys. Rev. C **44**, 1289 (1991).

[7] R. M. Id Betan, A. T. Kruppa, T. Vertse, Phys. Rev. C **97**, 024307 (2018).

[8] S. A. Rakityansky and N. Elander, J. Math. Phys. **54**, 122112 (2013).

[9] S. A. Rakityansky, S. N. Ershov, and T. J. Tshipi, Int. J. Mod. Phys. E **28**, 1950083 (2019).

[10] R. G. Newton, *Scattering Theory of Wave and Particles* (McGraw-Hill, New York, 1966).

[11] R. G. Newton, J. Math. Phys. **2**, 188 (1961).

[12] H. M. Nussenzveig, Nucl. Phys. **11**, 499 (1959).

[13] J. Bang, S. N. Ershov, F. A. Gareev, and G. S. Kazacha, Nucl. Phys. A **339**, 89 (1980).

[14] D. Gaspard, J. Math. Phys. **59**, 112104 (2018).

[15] J. Humblet, Ann. Phys. (NY) **155**, 461 (1984).

[16] H. Buchholz, *The Confluent Hypergeometric Function* (Springer-Verlag, Berlin, Heidelberg, New York, 1969).

[17] K. S. Kölbig, Comp. Phys. Commun. **4**, 221 (1972).

[18] F. W. J. Olver, D. W. Lozier, R. F. Boisvert, and C. W. Clark, *NIST Handbook of Mathematical Functions*, 1st ed. (NIST, New York, 2010).

[19] R. P. Boas, *Invitation to Complex Analysis* (Random House, New York, 1987).

[20] W. H. Press, S. A. Teukolsky, and W. T. Vetterling, *Numerical Recipes in Fortran 77*, 2nd ed. (Cambridge University Press, New York, 1997).